Measuring the Lower Critical Field of Superconductors Using Nitrogen-Vacancy Centers in Diamond Optical Magnetometry

K.R. Joshi,[1,2] N.M. Nusran,[1,2] M.A. Tanatar,[1,2] Kyuil Cho,[1,2] W.R. Meier,[1,2] S.L. Bud'ko,[1,2] P.C. Canfield,[1,2] and R. Prozorov[1,2,*]

[1] *Ames Laboratory, Ames, Iowa 50011, USA*

[2] *Department of Physics & Astronomy, Iowa State University, Ames, Iowa 50011, USA*

(Received 27 June 2018; revised manuscript received 5 November 2018; published 17 January 2019)

The lower critical magnetic field, H_{c1}, of superconductors is measured by optical magnetometry using ensembles of nitrogen-vacancy centers in diamond. The technique is minimally invasive and allows accurate detection of the vector magnetic field with subgauss sensitivity and submicrometer spatial resolution. These capabilities are used for detailed characterization of the first vortex penetration into superconducting samples from the corners. Aided by the revised calculations of the effective demagnetization factors of actual cuboid-shaped samples, these measurements provide precise determination of H_{c1} and the related absolute value of the London penetration depth, λ. We apply this method to three well-studied superconductors: optimally doped $Ba(Fe_{1-x}Co_x)_2As_2$, stoichiometric $CaKFe_4As_4$, and the high-T_c cuprate $YBa_2Cu_3O_{7-\delta}$. Our results compared well with the values of λ obtained with other techniques, thus adding another noninvasive and sensitive method to measure these important parameters of superconductors.

DOI: 10.1103/PhysRevApplied.11.014035

I. INTRODUCTION

Superconductors remain a focus of intense research due to their unusual properties and potential in applications. Cuprates [1] and, more recently, iron-based superconductors [2] are of particular interest due to their high superconducting transition temperature, T_c, apparently unconventional pairing mechanism [3,4], and rich interplay of magnetism and superconductivity, including their coexistence in the bulk [5–8].

One of the fundamentally important characteristics of a superconductor is the superfluid density, which determines the screening of an external magnetic field and is experimentally evaluated from the absolute value of the London penetration depth $\lambda(T)$. Accurate measurements of the lower (also known as the "first") critical field, H_{c1}, can be used to obtain λ directly; see Eq. (1). These measurements, however, are not simple. The nonspherical shape of the experimental samples leads to distortion of the magnetic fields at sample edges and necessitates vector-magnetic-field mappings with high spatial resolution of the order of λ, typically in the submicrometer range. This task was approached by use of local probes of magnetic induction, such as miniature Hall probes [9–11], miniature superconducting quantum-interference devices [12] and magnetic force microscopes [13], with spatial resolution in the micrometer range and sensitivity to a single component of the vector magnetic field.

Among several factors for accurate measurements of H_{c1}, three are the most important: (i) the "probe" has to be noninvasive so that the local magnetic environment is not disturbed, (ii) it has spatial resolution comparable to λ, and (iii) the demagnetization corrections due to a particular sample geometry or shape should be accounted for properly to facilitate proper determination of H_{c1} from measured H_p. Magnetic sensing probes based on nitrogen-vacancy (N-V) centers in diamond satisfy the first two requirements. The magnetic moment of the N-V center itself is of the order of μ_B, and thus minimally perturbs the original magnetic state of the measured specimen. Submicrometer spatial resolution can be achieved even with a N-V ensemble (as used here; see Sec. II for details), with a probe of 500-nm diameter and 20-nm thickness [14–18]. Furthermore, the ability to resolve the vector components of the magnetic induction provides better understanding of how the flux enters the sample.

In this work, we present a novel scheme for accurate measurements of H_{c1} of type-II superconductors using the N-V centers in diamond as an optical probe of local vector magnetic induction. Three different superconductors are measured, including the high-T_c cuprate $YBa_2Cu_3O_{7-\delta}$ (YBCO) and iron-based superconductors

*prozorov@iastate.edu

$Ba(Fe_{1-x}Co_x)_2As_2$ and $CaKFe_4As_4$, to demonstrate the performance of this technique. These materials are subjects of active current research [19,20]. To deduce H_{c1}, we use modified demagnetization factors derived for realistic three-dimensional geometries and also compare our results with results when demagnetization factors calculated from infinite geometries are used [21].

A. Lower critical magnetic field

The lower (first) critical field, H_{c1}, is one of the important fundamental parameters characterizing any type-II superconductor [22]. Above this field, Abrikosov vortices become energetically favorable and start entering the sample from the edges. Importantly, H_{c1} is related to two fundamental length scales, the London penetration depth, λ, and the coherence length ξ, as follows [23]:

$$H_{c1} = \frac{\phi_0}{4\pi\lambda^2}\left(\ln\frac{\lambda}{\xi} + 0.497\right). \quad (1)$$

ξ enters Eq. (1) only as a logarithm and there are other more-direct and more-sensitive ways to determine it experimentally [e.g., from the upper critical field, $H_{c2} = \phi_0/\left(2\pi\xi^2\right)$, where $\phi_0 = 2.07 \times 10^{-15}$ Wb is magnetic flux quantum]. Thus, the London penetration depth λ is often estimated with Eq. (1) if H_{c1} is experimentally given. In terms of the numerical values, for example, for the $Ba(Fe_{1-x}Co_x)_2As_2$ iron-based superconductor studied here [5,24], $\xi \approx 2.3$ nm and $\lambda \approx 200$ nm, so $\kappa = \lambda/\xi \approx 87$, which gives $H_{c1} \approx 200$ Oe and $H_{c2} \approx 60$ T. For optimally doped YBCO [25–27], $\xi \approx 1.6$ nm, $\lambda \approx 140$–160 nm, $\kappa \approx 80$–100, $H_{c1} \approx 350$–400 Oe, and $H_{c2} \approx 120$ T.

In practice, use of Eq. (1) to determine H_{c1} has two major difficulties: (i) the existence of various surface barriers [28–30] that inhibit the penetration of a magnetic field, hence leading to overestimation of H_{c1}, and (ii) the distortion of the magnetic field around the actual, finite-size sample that leads to underestimation of H_{c1}. Therefore, the experimentally detected onset of the magnetic field penetration, denoted here as H_p, coincides with H_{c1} only in the case of an infinite slab in a parallel magnetic field and no surface barrier, conditions that are almost impossible to achieve in experiments. However, analysis shows that H_p is directly proportional to H_{c1} with the appropriate geometric conversion factor [30,31]. Several previous studies analyzed the situation and now most experimentalists follow the numerical results published by Brandt [30,31], who used approximate nonlinear $E(j)$ characteristics to estimate the connection between H_p and H_{c1}. Here it is important to understand how H_p is defined.

In Brandt's picture, illustrated in Fig. 1, for samples with a rectangular cross section $2a \times 2c$ (see Fig. 2) with a magnetic field applied along the c axis, vortices start forming at the corners [where the local field is highest, Fig. 1(b)] and propagate as nearly straight segments cutting the corners

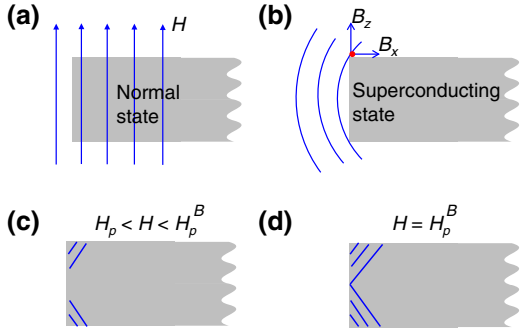

FIG. 1. (a) Applied magnetic field fully penetrating the superconductor in its normal state, (b) total expulsion of the magnetic flux by the superconductor in its superconducting state, (c) magnetic field entering from the corners of the sample at an angle of approximately 45°, and (d) Brandts' scenario when the applied magnetic field is equal to H_p^B. (See the text for details.)

at approximately 45° [Fig. 1(c)]. When the top and bottom segments meet in the middle of the side [at the "equator," Fig. 1(d)], the vortex enters the sample completely. At this value of the applied field, which we denote as H_p^B, the magnetization, $M(H)$, reaches maximum amplitude and $H_p^B \approx H_{c1}\tanh\sqrt{\alpha c/a}$, where $\alpha = 0.36$ for an infinite (in the b direction) strip or $\alpha = 0.67$ for disks of radius a [30]. At this field a significant volume of the sample is already occupied by vortices (from the corner cutting) and the local magnetic field at the corners has far exceeded H_{c1}.

An alternative definition of H_p is based on the deviation of the local magnetic induction from zero or the total magnetic moment from linear $M(H)$ behavior. In practice, the local magnetic induction, B, is measured outside the sample, on its surface close to the sample edge. The external magnetic field expelled by the sample leaks into the sensor,

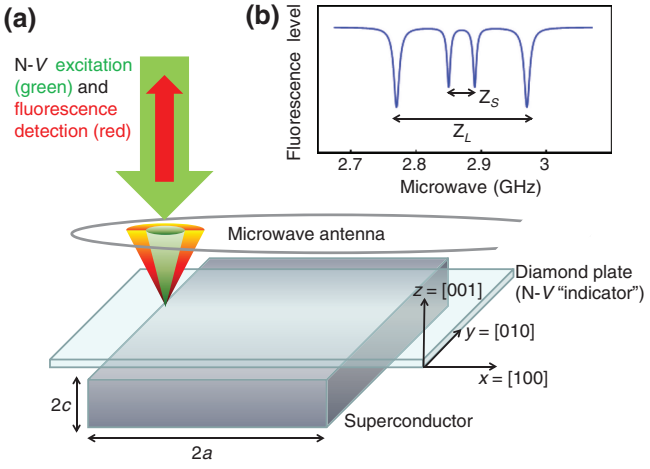

FIG. 2. (a) The key components of the N-V sensing setup (b) ODMR spectrum for a local magnetic field vector with two components, $\vec{B} = (B_x, 0, B_z)$. (See the text for details.)

so measured $B(H)$ is always nonzero, but is still linear in H and deviates from linearity when vortices start to penetrate the sample from the corners, which can be detected as the onset of the flux penetration field H_p [11,32]. A similar estimate can be obtained from the $M(H)$ curves detecting the deviation from linear behavior on application of a magnetic field after cooling in zero field [33]. Another version of this approach is to look for the remnant flux trapped inside the superconductor, which becomes nonzero when a lower critical field is reached in any part of the sample when vortices penetrated and became trapped due to ubiquitous pinnings [34]. In all these scenarios, the lower critical field should be obtained with the appropriate effective demagnetization factor, N:

$$H_p = H_{c1}\,(1 + N\chi)\,, \tag{2}$$

where χ is the "intrinsic" magnetic susceptibility of the material (i.e., in an "ideal" sample with no demagnetization and surface barriers), which can be taken to be equal to -1 for a robust superconductor at most temperatures below T_c [for an infinite slab of width $2w$ in a parallel field, $\chi = \lambda/w \tanh(w/\lambda) - 1$, and it is straightforward to check that χ is still less than -0.995 even at $T/T_c = 0.99$].

Unfortunately, most previous studies that used local measurements of the onset of magnetic flux penetration obtained with, for example, miniature Hall probes [11,32,34] analyzed the data with Brandt's formulas for H_p^B and not with the (more correct in this case) H_p from Eq. (2).

B. Effective demagnetizing factors

To use H_p to determine H_{c1}, the effective demagnetizing factor, N, has to be calculated for a specific sample geometry. Strictly speaking, N is defined only for ellipsoidal samples, which is of little practical use for typical samples of a cuboidal (rectangular-plate) shape. Yet, it is possible to introduce effective demagnetizing factors that were calculated in several previous studies, including the studies by Brandt previously cited, since his estimate of H_p^B implicitly includes the effective N [31]. As we recently showed from a full three-dimensional finite-element analysis [21], Brandt provided very accurate expressions for demagnetizing factors in cases of infinite strips or disks of rectangular cross section; see Eq. (7) in Ref. [31]. However, we also found that the effective demagnetizing factors for finite cuboids are quite different from those for infinite two-dimensional (2D) strips and, therefore, the whole method of estimating H_{c1} from magnetic measurements should be revisited. This is the subject of the present work.

Although we can calculate the effective demagnetization factor with arbitrary precision for a sample of any shape, it is always useful to have simple, but accurate-enough formulas [21]. A good approximation for a $2a \times 2b \times 2c$ cuboid in a magnetic field along the c direction is given by [21]

$$N^{-1} = 1 + \frac{3}{4}\frac{c}{a}\left(1 + \frac{a}{b}\right). \tag{3}$$

Having samples of rectangular cross section is problematic from point of view of the uncertainty in demagnetization effects, but it is advantageous in terms of the absence of surface barriers, because now magnetic flux penetrates from the corners and not parallel to the extended flat surfaces, which is how surface barriers are formed [28]. Moreover, the "geometric barrier" that essentially involves the flux corner penetration described above [30,31] is not relevant if the onset of nonlinearity is detected near the sample edge.

II. EXPERIMENT

A. Optical magnetic sensing using N-V centers in diamond

The vector magnetic induction on the sample surface is measured by optical magnetometry based on N-V centers in diamond. Specifically, the optically detected magnetic resonance (ODMR) of Zeeman-split energy levels in N-V centers, proportional to a local magnetic field, is measured [35]. The magnetosensing using N-V centers has several important advantages for measurements of delicate effects in superconductors: (i) it is minimally invasive (the magnetic moment of the probe itself is on the order of a few Bohr magnetons and hence has a negligible effect on the measured magnetic fields); (ii) it has sufficient spatial resolution (submicrometer spatial mapping can be achieved even with the ensemble mode of N-V sensing); (iii) it is capable of measuring vector magnetic induction [36]. This is particularly important as the detection of flux penetration depends on the location, and magnetic field lines deviate significantly from the direction of the applied field [21].

Measurement protocols, experimental schematics, and deconvolution of the ODMR spectrum into magnetic field components are discussed in detail in our previous work in which the spatial structure of the Meissner state in various superconductors was studied [36]. Here we focus particularly on measurements of the lower critical field, H_{c1}, and summarize the key experimental details for the completeness.

To measure a local magnetic induction, a magneto-optical "indicator" ($1.5 \times 1 \times 0.04$ mm^3 diamond plate with embedded N-V centers) is placed on top of the superconducting sample with its N-V-active side facing the sample surface. On the "active" side, N-V centers are created within approximately 20 nm from the surface of a single-crystal diamond plate with commercial protocols that involve nitrogen-ion implantation, electron irradiation, and high-temperature annealing in a high vacuum. The

diamond plate has a (100) crystal surface and [100] edges. Therefore, N-V centers are oriented along all four [111] diamond axes, which define the directions of the magnetic field sensing. As a result, possible Zeeman splittings in a random ensemble of N-V centers in (indeed, a single crystal of) diamond are given by $2\gamma_e|\vec{B}\cdot\hat{d}|$, where $\gamma_e \approx 2.8$ MHz/G is the gyromagnetic ratio of the N-V-center electronic spin and $\hat{d}$ is a unit vector along any of the four diamond axes. In a magnetic field along the $\hat{z}$ direction, that is, $\vec{B} = (0, 0, B_z)$, all possible N-V orientations result in the same splitting:

$$Z = \frac{2\gamma_e}{\sqrt{3}} \approx 3.233 \text{ MHz/G}.$$

However, if the magnetic field has two components such that $\vec{B} = (B_x, 0, B_z)$, the N-V ensemble will result in two pairs of Zeeman splitting:

$$Z_{L,S} = Z|B_z \pm B_x|,$$

where Z_L (Z_S) refers to larger (smaller) Zeeman splitting. An example of such two pairs of ODMR splitting is shown in Fig. 2(b).

B. Experimental details

1. Experimental setup

The experimental setup is based on an Attocube attoAFM/CFM system and includes a confocal microscope optimized for N-V fluorescence detection inside a helium cryostat with optical parts in vacuum and the sample placed on a temperature-controlled cold stage. A schematic of the experiment is shown in Fig. 2(a). The objective is focused on the N-V centers in an optically transparent diamond plate so that the convolution of the diffraction-limited confocal volume with the N-V distribution essentially leads to a disk-shaped sensing volume of thickness approximately 20 nm and diameter approximately 500 nm. The diamond plate is placed directly on top of a flat sample surface covering the edge and with the N-V-active side facing the sample. More importantly, the superconducting sample edges are carefully aligned with diamond edges so that when the superconductor is in the Meissner state the vector magnetic field at the probing point will have no component along the [010] diamond-crystal direction. This symmetry of placement guarantees only two pairs of Zeeman splitting in the ODMR. A 50× confocal-microscope objective is used both for green-laser excitation and red-fluorescence collection. Microwave radiation with a very small amplitude is applied with a single-turn 50-μm-diameter silver wire.

2. Temperature variation during measurements

The laser and microwave power used in these experiments are approximately 500 μW and less than 0 dBm, respectively. While no noticeable effect is observed due to the laser, microwave excitation results in a small change in the base temperature fluctuating between 4.2 and 4.3 K. Therefore, all our experiments are performed at 4.5 K with active temperature control keeping the temperature stable within approximately 10 mK. These fluctuations are much lower than reported in Ref. [37], probably because our microwave-loop-antenna geometry is more optimized for the experiment.

3. Spatial resolution

Spatial resolution of the probe is governed by the optical diffraction limit, resulting in lateral resolution of approximately 500 nm. One possibility to increase the lateral resolution is to incorporate super-resolution imaging techniques [38,39]. Another possibility is to use nanoscale scanning N-V probes [40–42]. Magnetic imaging of individual Abrikosov vortices was demonstrated with scanning single N-V probes in Refs. [43,44]. The imaged superconducting materials in those studies were field cooled to the superconducting state in the presence of a weak external background magnetic field to form a well-isolated vortex distribution.

4. Integration time

In our H_{c1} measurements, for each data point (a given position and external magnetic field), the ODMR spectrum is obtained for a 50–100-MHz scan range averaged for ten repetitions. The typical total integration time per data point is 5–10 min. To speed up the experiments, one could use adaptive protocols to modify or optimize the scan range and number of averages according to the previous measurement results. Another possibility is to incorporate real-time lock-in-detection techniques [45].

5. Samples

All samples are precharacterized by various thermodynamic and transport techniques (see, e.g., Ref. [46]) and imaged by scanning electron microscopy, and only samples with well-defined surfaces and edges, as shown in Fig. 3(a), are selected for further measurements.

III. MEASUREMENTS OF THE LOWER CRITICAL FIELD

The experimental protocol for measurements of H_{c1} is as follows:

(a) The sample is cooled to the target temperature below T_c in the absence of a magnetic field (zero-field cooling, ZFC). Then a small magnetic field (10 Oe in our case, much smaller than the 200–400 Oe expected for H_{c1} at low temperatures as discussed in Sec. I) is applied and ODMR signals are recorded at different points

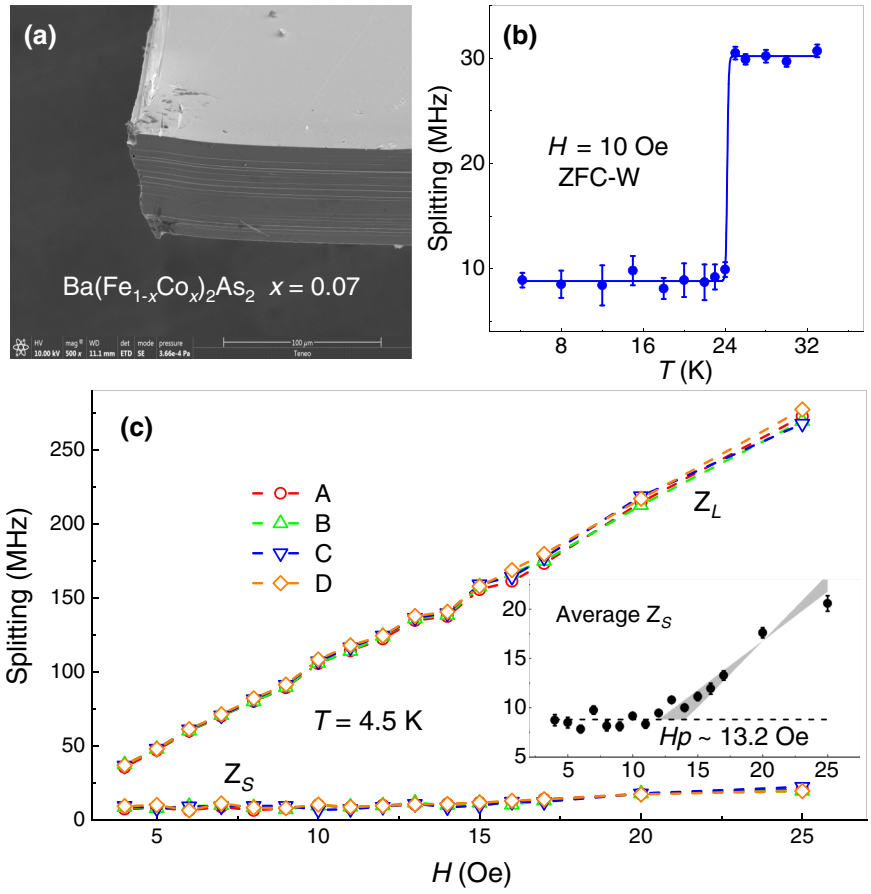

FIG. 3. (a) Scanning-electron-microscope image of the measured single crystal of $Ba(Fe_{1-x}Co_x)_2As_2$, $x = 0.07$ (b) Detection of the superconducting phase transition at $T_c \approx 24$ K in the "warming" curve upon zero-field-cool (ZFC-W). Each data point in the plot is obtained from a total integration time of the ODMR of 4 min. Error bars represent the standard errors extracted from the double-Lorentz-function fitting parameters for the dip position (not shown here). (c) H_{c1} measurements of this sample at 4.5 K. Zeeman splittings measured at four different points (A, B, C, and D) near the edge as a function of increasing magnetic field applied after zero-field cooling (ZFC). The four-point-averaged signal of Z_S is shown in the inset; a clear "change" at $H_p = 13.2 \pm 1$ Oe is observed. The shaded area visually captures the spread of measurements after this change, from which the error of H_p is determined.

along the line perpendicular to the sample edge. Measured ODMR splittings are then converted into the magnetic induction values as described above. This, combined with direct visualization of the sample through a transparent diamond plate, allows accurate determination of the location of the sample edge and provides information about sample homogeneity. The quality of the superconductor is also verified by the sharpness of the transition detected by the ODMR splitting recorded as a function of temperature at any fixed point over the sample; see, for example, Fig. 3(b).

(b) After this initial preparation and edge identification, the magnetic field is removed and the sample is warmed up to above T_c and then cooled back down to a target temperature, thereby resetting it to the genuine superconducting state with no trapped magnetic field inside. A point inside and over the sample, but close to the edge, is chosen and ODMR spectra are recorded as a function of the external magnetic field, which is applied incrementally in small steps. At each step, the superconducting magnet is switched to a persistent mode to ensure stability of the magnetic field. The deviation from the linear behavior in Z_S is then detected and recorded as the field of first flux penetration, H_p.

(c) With use of Eqs. (2), (3), and (1), H_{c1} and the London penetration depth λ are evaluated. This procedure is repeated at several locations along the edge to ensure objectivity of the results.

IV. RESULTS AND DISCUSSION

To illustrate the method described, we measure H_{c1} and evaluate the London penetration depth, λ, in three different superconducting materials.

A. $Ba(Fe_{1-x}Co_x)_2As_2$, $x = 0.07$

A well-characterized optimally doped single crystal of $Ba(Fe_{1-x}Co_x)_2As_2$, $x = 0.07$, of cuboidal shape with dimensions $1.0 \times 1.2 \times 0.05$ mm^3 was selected. The scanning-electron-microscope image in Fig. 3(a) shows a well-defined rectangular corner with flat clean surface and straight edges. The superconducting transition temperature, $T_c \approx 24$ K, determined with a conventional magnetometer, is consistent with our ODMR measurements at the location on the sample surface inside the sample as shown in Fig. 3(b). ODMR splittings at four different locations on the sample surface near the edge are labeled A, B, C, and D in Fig. 3(c). These four points are approximately 5 μm from neighboring points and each point is approximately 10 μm from the edge inside the sample. As discussed above, the two Zeeman splittings Z_L and Z_S correspond to linear combinations of horizontal (B_x) and

vertical (B_z) components of the magnetic induction. Notice excellent reproducibility of the results, indicating homogeneous superconducting properties of our sample. The inset in Fig. 3(c) shows the average (of four points) small splitting signal (Z_S). A clear onset of first flux penetration is determined at $H_p = 13.2 \pm 1$ Oe.

To understand the observed ODMR splittings, we consider Brandt's results of flux corner cutting and entering in the form of Abrikosov vortices at an angle of approximately 45° with respect to the corner. Therefore, the normal-to-the-sample-surface z component (along the applied field) and the longitudinal x component of the magnetic induction are approximately equal and proportional to the applied field. This linear relation continues with increasing applied field until the first flux penetration field, H_p, is reached. At this point, the angle of the magnetic flux at the sample edges deviates from 45°, trending more toward the $\hat{z}$ direction. This scenario can be phenomenologically modeled by our representing the magnetic induction components as $B_{z,x} = DH \pm \delta$ and $\delta = 0 + \alpha\theta(H - H_p)(H - H_p)^n$, where D is an effective demagnetization factor and $\theta(H)$ is a Heaviside step function. Because the larger splitting Z_L and the smaller splitting Z_S are proportional to the sum and difference of $B_{z,x}$ components, respectively, the change at H_p is reflected clearly in Z_S but not in Z_L. The Zeeman splittings observed in Fig. 3(c) can be understood with this model for the parameters: $D = 3.5$, $H_p = 13.2$, $\alpha = 0.6$, and $n = 1$. Hence, this provides experimental confirmation for Brandt's description of flux corner cutting and entering at an angle of approximately 45° with respect to the sides.

From the experimental value of H_p and the effective demagnetization factor for this particular sample, $N = 0.9168$, we obtain using Eq. (2), $H_{c1} = 158 \pm 12$ Oe. Using Eq. (1) and taking $\xi \approx 2.3$ nm, we obtain the final result, $\lambda = 226 \pm 10$ nm. This estimate for the penetration depth is comparable with the values obtained from other techniques such as muon spin relaxation (224 nm) [47] and magnetic force microscopy (245 nm) [48]. The agreement is quite remarkable and gives confidence in the validity of the technique developed. Table I summarizes all these estimates. Estimates obtained with Brandt's formulas are also given for comparison.

B. $CaKFe_4As_4$

The cuboid single crystal of stoichiometric $CaKFe_4As_4$ with dimensions of $1.01 \times 0.99 \times 0.01$ mm^3 is studied. The inset in Fig. 4(a) shows a sharp superconducting phase transition at $T_c \approx 34$ K. The average ODMR splitting, Z_S, near the sample edge as a function of the applied magnetic field clearly shows a break associated with the magnetic flux penetration at $H_p = 8.3 \pm 1.1$ Oe. The error here is determined visually by the shaded region that spans all measurement points. With use of Eqs. (2) and (3), this

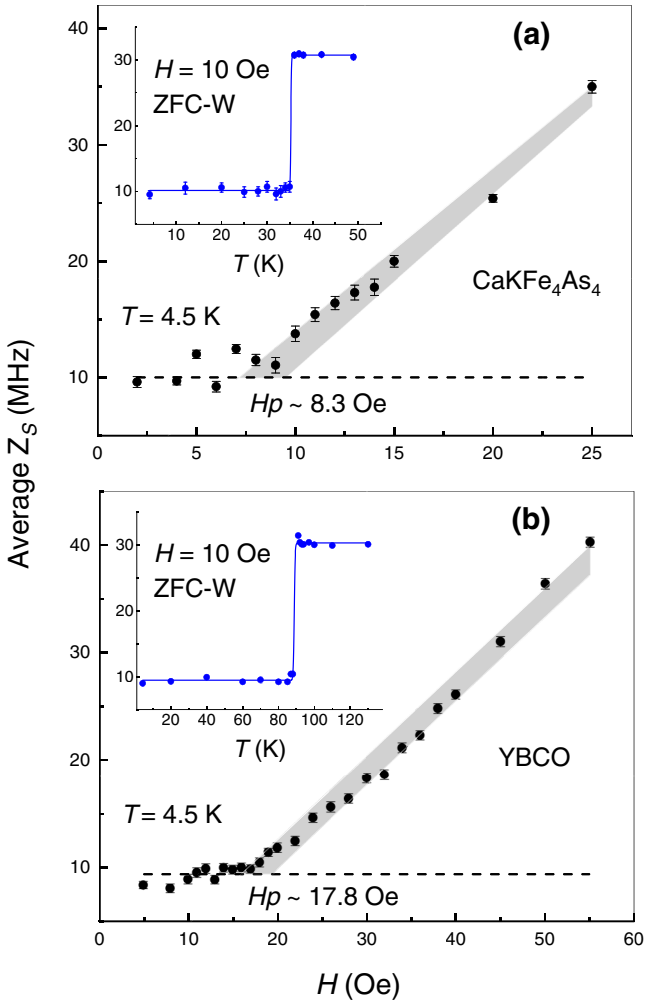

FIG. 4. Measurements of the field of first flux penetration, H_p, in single crystals of (a) $CaKFe_4As_4$ and (b) $YBa_2Cu_3O_{7-\delta}$. The insets show superconducting phase transitions at $T_c \approx 34$ K and 88 K, respectively. ZFC-W, zero-field-cool warming.

results in the estimation of $H_{c1} = 394 \pm 52$ Oe. Using Eq. (1) and $\xi \approx 2.15$ nm [46], we estimate $\lambda = 141 \pm 11$ nm. This result was used to calculate the superfluid density in Ref. [46], which is consistent with isotropic two-gap $s_\pm$ pairing state.

C. $YBa_2Cu_3O_{7-\delta}$

To look at a very different system, we also measure a single crystal of a well-known cuprate superconductor, YBCO. The sample dimensions are $0.5 \times 0.85 \times 0.017$ mm^3. The inset in Fig. 4(b) shows a sharp superconducting phase transition at $T_c \approx 88$ K. The clear break associated with the magnetic field of first flux penetration in the average Z_S versus H plot is observed at $H_p = 17.8 \pm 1.6$ Oe. With use of Eqs. (2) and (3), this leads to estimation of $H_{c1} = 344 \pm 31$ Oe. Using Eq. (1) and coherence length $\xi \approx 1.6$ nm [25,27], we estimate $\lambda \approx 156 \pm 8$ nm. All

TABLE I. Estimates for H_{c1} and λ. Here "2D" refers to values obtained with Brandt's formulas.

Superconductor	T_c (K)	H_{c1}^{2D}(G)	λ^{2D} (nm)	H_{c1} (G)	λ (nm)	λ (nm) from the literature
$Ba(Fe_{1-x}Co_x)_2As_2$, $x = 0.07$	24.3	102 ± 8	288 ± 12	158 ± 12	226 ± 10	270, 245, 224 [47–49]
$CaKFe_4As_4$	34	139 ± 18	251 ± 18	394 ± 52	141 ± 11	208, 187 [50]
YBCO	88.3	163 ± 15	236 ± 12	344 ± 31	156 ± 8	146, 160, 155, 149 [26,51–53]

estimates, including values obtained with Brandt's formulas and from other techniques, are summarized in Table I. Once again, good agreement is seen between our estimates and the values reported in the literature obtained with other techniques, such as muon spin relaxation (155 nm) [52], microwave-cavity perturbation (160 nm) [51], and use of a tunnel-diode resonator (140 nm) [26].

V. CONCLUSIONS

In summary we use N-V centers in diamond for sensing of the optical vector magnetic field at low temperatures to measure the lower critical field, H_{c1}, in type-II superconductors. The minimally invasive nature and optical-diffraction-limited small size of the probe make a N-V sensor ideal for this purpose. The capability of resolving vector components provides a unique advantage, which allows direct verification of Brandt's model of magnetic flux penetration that proceeds via corner cutting by vortices at an angle of approximately 45° with respect to the edges. We apply this technique to three different superconductors: optimally doped $Ba(Fe_{1-x}Co_x)_2As_2$, $x = 0.07$, stoichiometric $CaKFe_4As_4$, and the high-T_c cuprate YBCO. The London penetration depths evaluated from the H_{c1} values obtained are in good agreement with values in the literature. Our approach is a very useful noninvasive way to estimate the absolute value of London penetration depth $\lambda(T)$, needed to obtain temperature-dependent superfluid density, a quantity directly comparable to theoretical calculations.

ACKNOWLEDGMENTS

This work was supported by the U.S. Department of Energy, Office of Science, Basic Energy Sciences, Materials Science and Engineering Division. The research was performed at Ames Laboratory, which is operated for the U.S. Department of Energy by Iowa State University under Contract No. DE-AC02-07CH11358. W.M. was supported by the Gordon and Betty Moore Foundation's EPiQS Initiative through Grant No. GBMF4411.

[1] J. G. Bednorz and K. A. Müller, Possible high T_c superconductivity in the Ba-La-Cu-O system, Z. Phys. B **64**, 189 (1986).

[2] Yoichi Kamihara, Takumi Watanabe, Masahiro Hirano, and Hideo Hosono, Iron-based layered superconductor $La[O_{1-x}F_x]FeAs$ ($x = 0.05 - 0.12$) with $T_c = 26$ K, J. Am. Chem. Soc. **130**, 3296 (2008).

[3] C. C. Tsuei and J. R. Kirtley, Pairing symmetry in cuprate superconductors, Rev. Mod. Phys. **72**, 969 (2000).

[4] I. I. Mazin, Superconductivity gets an iron boost, Nature **464**, 183 (2010).

[5] Paul C. Canfield and Sergey L. Bud'ko, FeAs-Based superconductivity: A case study of the effects of transition metal doping on $BaFe_2As_2$, Annu. Rev. Condens. Matter Phys. **1**, 27 (2010).

[6] David C. Johnston, The puzzle of high temperature superconductivity in layered iron pnictides and chalcogenides, Adv. Phys. **59**, 803 (2010).

[7] G. R. Stewart, Superconductivity in iron compounds, Rev. Mod. Phys. **83**, 1589 (2011).

[8] R. M. Fernandes, A. V. Chubukov, and J. Schmalian, What drives nematic order in iron-based superconductors? Nat. Phys. **10**, 97 (2014).

[9] M. Konczykowski, F. Holtzberg, and P. Lejay, Local Hall probe magnetometry: A new technique for investigation of magnetic flux penetration, exclusion and trapping in HTSC, Supercond. Sci. Technol. **4**, S331 (1991).

[10] C. Putzke, P. Walmsley, J. D. Fletcher, L. Malone, D. Vignolles, C. Proust, S. Badoux, P. See, H. E. Beere, D. A. Ritchie, S. Kasahara, Y. Mizukami, T. Shibauchi, Y. Matsuda, and A. Carrington, Anomalous critical fields in quantum critical superconductors, Nat. Commun. **5**, 5679 (2014).

[11] T. Klein, D. Braithwaite, A. Demuer, W. Knafo, G. Lapertot, C. Marcenat, P. Rodière, I. Sheikin, P. Strobel, A. Sulpice, and P. Toulemonde, Thermodynamic phase diagram of $Fe(Se_{0.5}Te_{0.5})$ single crystals in field sup to 28 tesla, Phys. Rev. B **82**, 184506 (2010).

[12] Clifford W. Hicks, Thomas M. Lippman, Martin E. Huber, James G. Analytis, Jiun-Haw Chu, Ann S. Erickson, Ian R. Fisher, and Kathryn A. Moler, Evidence for a Nodal Energy Gap in the Iron-Pnictide Superconductor LaFePO from Penetration Depth Measurements by Scanning SQUID Susceptometry, Phys. Rev. Lett. **103**, 127003 (2009).

[13] Lan Luan, Ophir M. Auslaender, Thomas M. Lippman, Clifford W. Hicks, Beena Kalisky, Jiun-Haw Chu, James G. Analytis, Ian R. Fisher, John R. Kirtley, and Kathryn A. Moler, Local measurement of the penetration depth in the pnictide superconductor $Ba(Fe_{0.95}Co_{0.05})_2As_2$, Phys. Rev. B **81**, 100501 (2010).

[14] Francesco Casola, Toeno van der Sar, and Amir Yacoby, Probing condensed matter physics with magnetometry based on nitrogen-vacancy centres in diamond, Nat. Rev. Mater. **3**, 17088 (2018).

[15] J.-P. Tetienne, N. Dontschuk, D. A. Broadway, A. Stacey, D. A. Simpson, and L. C. L. Hollenberg, Quantum imaging of current flow in graphene, Sci. Adv. **3**, e1602429 (2017).

[16] L. Rondin, J.-P. Tetienne, T. Hingant, J.-F. Roch, P. Maletinsky, and V. Jacques, Magnetometry with nitrogen-vacancy defects in diamond, Rep. Prog. Phys. **77**, 056503 (2014).

[17] Romana Schirhagl, Kevin Chang, Michael Loretz, and Christian L. Degen, Nitrogen-vacancy centers in diamond: Nanoscale sensors for physics and biology, Annu. Rev. Phys. Chem. **65**, 83 (2014).

[18] L. M. Pham, D. Le Sage, P. L. Stanwix, T. K. Yeung, D. Glenn, A. Trifonov, P. Cappellaro, P. R. Hemmer, M. D. Lukin, H. Park, A. Yacoby, and R. L. Walsworth, Magnetic field imaging with nitrogen-vacancy ensembles, New J. Phys. **13**, 045021 (2011).

[19] Akira Iyo, Kenji Kawashima, Tatsuya Kinjo, Taichiro Nishio, Shigeyuki Ishida, Hiroshi Fujihisa, Yoshito Gotoh, Kunihiro Kihou, Hiroshi Eisaki, and Yoshiyuki Yoshida, New-structure-type Fe-based superconductors: $CaAFe_4As_4$ ($A = K$, Rb, Cs) and $SrAFe_4As_4$ ($A =$ Rb, Cs), J. Am. Chem. Soc. **138**, 3410 (2016).

[20] W. R. Meier, T. Kong, U. S. Kaluarachchi, V. Taufour, N. H. Jo, G. Drachuck, A. E. Böhmer, S. M. Saunders, A. Sapkota, A. Kreyssig, M. A. Tanatar, R. Prozorov, A. I. Goldman, F. F. Balakirev, Alex Gurevich, S. L. Bud'ko, and P. C. Canfield, Anisotropic thermodynamic and transport properties of single-crystalline $CaKFe_4As_4$, Phys. Rev. B **94**, 064501 (2016).

[21] R. Prozorov and V. G. Kogan, Effective Demagnetizing Factors of Diamagnetic Samples of Various Shapes, Phys. Rev. Appl. **10**, 014030 (2018).

[22] M. Tinkham, *Introduction to Superconductivity*, 2nd ed. Dover Books on Physics (Dover Publications, New York, 2004).

[23] Chia-Ren Hu, Numerical constants for isolated vortices in superconductors, Phys. Rev. B **6**, 1756 (1972).

[24] R. Prozorov and V. G. Kogan, London penetration depth in iron-based superconductors, Rep. Prog. Phys. **74**, 124505 (2011).

[25] K. E. Gray, D. H. Kim, B. W. Veal, G. T. Seidler, T. F. Rosenbaum, and D. E. Farrell, High anisotropy and a dimensionality crossover in the irreversibility behavior of oxygen-deficient $YBa_2Cu_3O_{7-y}$, Phys. Rev. B **45**, 10071 (1992).

[26] R. Prozorov, R. W. Giannetta, A. Carrington, P. Fournier, R. L. Greene, P. Guptasarma, D. G. Hinks, and A. R. Banks, Measurements of the absolute value of the penetration depth in high-T_c superconductors using a low T_c superconductive coating, Appl. Phys. Lett. **77**, 4202 (2000).

[27] T. Sekitani, N. Miura, S. Ikeda, Y. H. Matsuda, and Y. Shiohara, Upper critical field for optimally-doped $YBa_2Cu_3O_{7-\delta}$, Physica B: Condensed Matter **346–347**, 319 (2004).

[28] C. P. Bean and J. D. Livingston, Surface Barrier in Type-II Superconductors, Phys. Rev. Lett. **12**, 14 (1964).

[29] E. H. Brandt, The flux-line lattice in superconductors, Rep. Prog. Phys. **58**, 1465 (1995).

[30] Ernst Helmut Brandt, Geometric barrier and current string in type-II superconductors obtained from continuum electrodynamics, Phys. Rev. B **59**, 3369 (1999).

[31] E. H. Brandt, Geometric edge barrier in the Shubnikov phase of type-II superconductors, Low Temp. Phys. **27**, 723 (2001).

[32] R. Okazaki, M. Konczykowski, C. J. van der Beek, T. Kato, K. Hashimoto, M. Shimozawa, H. Shishido, M. Yamashita, M. Ishikado, H. Kito, A. Iyo, H. Eisaki, S. Shamoto, T. Shibauchi, and Y. Matsuda, Lower critical fields of superconducting $PrFeAsO_{1-y}$ single crystals, Phys. Rev. B **79**, 064520 (2009).

[33] M. Abdel-Hafiez, J. Ge, A. N. Vasiliev, D. A. Chareev, J. Van de Vondel, V. V. Moshchalkov, and A. V. Silhanek, Temperature dependence of lower critical field $H_{c1}(T)$ shows nodeless superconductivity in FeSe, Phys. Rev. B **88**, 174512 (2013).

[34] Z. Pribulova, T. Klein, J. Kacmarcik, C. Marcenat, M. Konczykowski, S. L. Bud'ko, M. Tillman, and P. C. Canfield, Upper and lower critical magnetic fields of superconducting $NdFeAsO_{1-x}F_x$ single crystals studied by Hall-probe magnetization and specific heat, Phys. Rev. B **79**, 020508 (2009).

[35] L. Rondin, J. P. Tetienne, S. Rohart, A. Thiaville, T. Hingant, P. Spinicelli, J. F. Roch, and V. Jacques, Stray-field imaging of magnetic vortices with a single diamond spin, Nat. Commun. **4**, 2279 (2013).

[36] N. M. Nusran, K. R. Joshi, K. Cho, M. A. Tanatar, W. R. Meier, S. L. Budko, P. C. Canfield, Y. Liu, T. A. Lograsso, and R. Prozorov, Spatially-resolved study of the Meissner effect in superconductors using NV-centers-in-diamond optical magnetometry, New J. Phys. **20**, 043010 (2018).

[37] Dominik Rohner, Lucas Thiel, Benedikt Müller, Mark Kasperczyk, Reinhold Kleiner, Dieter Koelle, and Patrick Maletinsky, Real-space probing of the local magnetic response of thin-film superconductors using single spin magnetometry, Sensors **18**, 3790 (2018).

[38] Eva Rittweger, Kyu Young Han, Scott E. Irvine, Christian Eggeling, and Stefan W. Hell, STED microscopy reveals crystal colour centres with nanometric resolution, Nature Photon. **3**, 144 (2009).

[39] Edward H. Chen, Ophir Gaathon, Matthew E. Trusheim, and Dirk Englund, Wide-field multispectral super-resolution imaging using spin-dependent fluorescence in nanodiamonds, Nano Lett. **13**, 2073 (2013).

[40] P. Maletinsky, S. Hong, M. S. Grinolds, B. Hausmann, M. D. Lukin, R. L. Walsworth, M. Loncar, and A. Yacoby, A robust scanning diamond sensor for nanoscale imaging with single nitrogen-vacancy centres, Nat. Nanotechnol. **7**, 320 (2012).

[41] Patrick Appel, Elke Neu, Marc Ganzhorn, Arne Barfuss, Marietta Batzer, Micha Gratz, Andreas Tschoepe, and Patrick Maletinsky, Fabrication of all diamond scanning probes for nanoscale magnetometry, Rev. Sci. Instrum. **87**, 063703 (2016).

[42] Tony X. Zhou, Rainer J. Stoehr, and Amir Yacoby, Scanning diamond NV center probes compatible with conventional AFM technology, Appl. Phys. Lett. **111**, 163106 (2017).

[43] L. Thiel, D. Rohner, M. Ganzhorn, P. Appel, E. Neu, B. Müller, R. Kleiner, D. Koelle, and P. Maletinsky, Quantitative nanoscale vortex imaging using a cryogenic quantum magnetometer, Nat. Nanotechnol. **11**, 677 (2016).

[44] M. Pelliccione, A. Jenkins, P. Ovartchaiyapong, C. Reetz, E. Emmanouilidou, N. Ni, and A. C. Bleszynski Jayich, Scanned probe imaging of nanoscale magnetism at cryogenic temperatures with a single-spin quantum sensor, Nat. Nanotechnol. **11**, 700 (2016).

[45] Rolf Simon Schoenfeld and Wolfgang Harneit, Real Time Magnetic Field Sensing and Imaging Using a Single Spin in Diamond, Phys. Rev. Lett. **106**, 030802 (2011).

[46] Kyuil Cho, A. Fente, S. Teknowijoyo, M. A. Tanatar, K. R. Joshi, N. M. Nusran, T. Kong, W. R. Meier, U. Kaluarachchi, I. Guillamón, H. Suderow, S. L. Bud'ko, P. C. Canfield, and R. Prozorov, Nodeless multiband superconductivity in stoichiometric single-crystalline $CaKFe_4As_4$, Phys. Rev. B **95**, 100502 (2017).

[47] T. J. Williams, A. A. Aczel, E. Baggio-Saitovitch, S. L. Bud'ko, P. C. Canfield, J. P. Carlo, T. Goko, H. Kageyama, A. Kitada, J. Munevar, N. Ni, S. R. Saha, K. Kirschenbaum, J. Paglione, D. R. Sanchez-Candela, Y. J. Uemura, and G. M. Luke, Superfluid density and field-induced magnetism in $Ba(Fe_{1-x}Co_x)_2As_2$ and $Sr(Fe_{1-x}Co_x)_2As_2$ measured with muon spin relaxation, Phys. Rev. B **82**, 094512 (2010).

[48] Lan Luan, Thomas M. Lippman, Clifford W. Hicks, Julie A. Bert, Ophir M. Auslaender, Jiun-Haw Chu, James G. Analytis, Ian R. Fisher, and Kathryn A. Moler, Local Measurement of the Superfluid Density in the Pnictide Superconductor $Ba(Fe_{1-x}Co_x)_2As_2$ across the Superconducting Dome, Phys. Rev. Lett. **106**, 067001 (2011).

[49] R. T. Gordon, H. Kim, N. Salovich, R. W. Giannetta, R. M. Fernandes, V. G. Kogan, T. Prozorov, S. L. Bud'ko, P. C. Canfield, M. A. Tanatar, and R. Prozorov, Doping evolution of the absolute value of the London penetration depth and superfluid density in single crystals of $Ba(Fe_{1-x}Co_x)_2As_2$, Phys. Rev. B **82**, 054507 (2010).

[50] Rustem Khasanov, William R. Meier, Yun Wu, Daixiang Mou, Sergey L. Bud'ko, Ilya Eremin, Hubertus Luetkens, Adam Kaminski, Paul C. Canfield, and Alex Amato, In-plane magnetic penetration depth of superconducting $CaKFe_4As_4$, Phys. Rev. B **97**, 140503 (2018).

[51] Dong-Ho Wu, W. L. Kennedy, C. Zahopoulos, and S. Sridhar, Characteristics and growth of single crystals of $Y_1Ba_2Cu_3O_7$ with superior microwave properties, Appl. Phys. Lett. **55**, 696 (1989).

[52] J. L. Tallon, C. Bernhard, U. Binninger, A. Hofer, G. V. M. Williams, E. J. Ansaldo, J. I. Budnick, and Ch. Niedermayer, In-Plane Anisotropy of the Penetration Depth Due to Superconductivity on the Cu-O Chains in $YBa_2Cu_3O_{7-\delta}$, $Y_2Ba_4Cu_7O_{15-\delta}$, and $YBa_2Cu_4O_8$, Phys. Rev. Lett. **74**, 1008 (1995).

[53] J. E. Sonier, R. F. Kiefl, J. H. Brewer, D. A. Bonn, J. F. Carolan, K. H. Chow, P. Dosanjh, W. N. Hardy, Ruixing Liang, W. A. MacFarlane, P. Mendels, G. D. Morris, T. M. Riseman, and J. W. Schneider, New Muon-Spin-Rotation Measurement of the Temperature Dependence of the Magnetic Penetration Depth in $YBa_2Cu_3O_{6.95}$, Phys. Rev. Lett. **72**, 744 (1994).